

Modulate and Reconstruct: Learning Hyperspectral Imaging from Misaligned Smartphone Views

Daniil Reutsky¹, Daniil Vladimirov^{2,3}, Yasin Mamedov^{2,3},
Georgy Perevozchikov¹, Nancy Mehta¹, Egor Ershov^{2,3,4}, and
Radu Timofte¹

¹JMU, Würzburg

²CRSI, Moscow

³MIRIAI, Moscow

⁴AXXX, Moscow

Abstract

Hyperspectral reconstruction (HSR) from RGB images is a fundamentally ill-posed problem due to severe spectral information loss. Existing approaches typically rely on a single RGB image, limiting reconstruction accuracy. In this work, we propose a novel multi-image-to-hyperspectral reconstruction (MI-HSR) framework that leverages a triple-camera smartphone system, where two lenses are equipped with carefully selected spectral filters. Our configuration, grounded in theoretical and empirical analysis, enables richer and more diverse spectral observations than conventional single-camera setups. To support this new paradigm, we introduce Doomer, the first dataset for MI-HSR, comprising aligned images from three smartphone cameras and a hyperspectral reference camera across diverse scenes. We show that the proposed HSR model achieves consistent improvements over existing methods on the newly proposed benchmark. In a nutshell, our setup allows 30% towards more accurately estimated spectra compared to an ordinary RGB camera. Our findings suggest that multi-view spectral filtering with commodity hardware can unlock more accurate and practical hyperspectral imaging solutions.

1 Introduction

Hyperspectral imaging provide dense spectral measurements at each spatial pixel forming a 3D cube $\mathbf{I}_{\text{HS}} \in \mathbb{R}^{h \times w \times n}$, where $n \gg 3$. This enables fine-grained analysis of material properties in applications ranging from remote sensing [1], to medical diagnostics [2], to historical preservation [3], to ISP improvement [4, 5], to food quality assessment [6, 7]. However, acquiring such high-dimensional data typically requires hardware expensive, bulky, and often reliant on time-consuming scanning thus

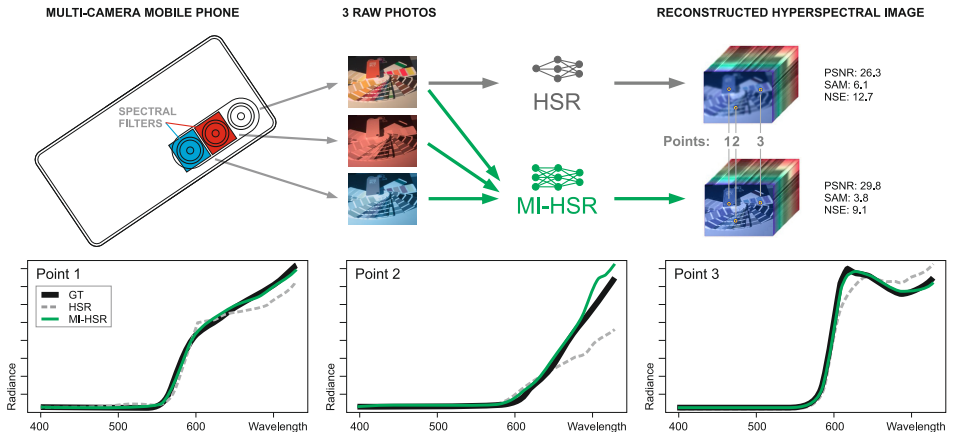


Figure 1: Proposed low-cost mobile spectral imaging system that transforms a standard smartphone into a spectrally diverse capture device via external filters on auxiliary cameras. This configuration enables simultaneous, multi-channel acquisition without internal hardware modification, supporting practical and scalable hyperspectral reconstruction.

fundamentally limiting the usability of hyperspectral imaging in dynamic or consumer settings.

An increasingly studied alternative is *hyperspectral reconstruction* (HSR): recovering \mathbf{I}_{HS} from an RGB observation $\mathbf{I}_{\text{RGB}} \in \mathbb{R}^{h \times w \times 3}$ captured via a sensor with spectral sensitivity matrix $\mathbf{S} \in \mathbb{R}^{3 \times n}$ under noise \mathbf{N} :

$$\mathbf{I}_{\text{RGB}}(x, y) = \mathbf{S} \cdot \mathbf{I}_{\text{HS}}(x, y) + \mathbf{N}(x, y).$$

This inverse problem is highly ill-posed and advances in deep learning-based HSR [8, 9], reconstructing \mathbf{I}_{HS} from a single RGB view remains fundamentally limited by the low spectral observability.

Several efforts have aimed to improve this observability. Learned or optimized multispectral filter arrays (MSFAs) [10], end-to-end spectral sensitivity learning [11], and joint sensor-network co-design [12] have all been proposed. However, these methods assume control over sensor hardware and manufacturing thus making them impractical for scalable or consumer-level deployment.

One underexplored but promising path is to leverage the multi-camera systems found in modern smartphones. These devices already include multiple rear cameras with different lenses and spectral sensitivities. In principle, such a setup can be treated as a low-cost, multi-spectral capture system thus capable of observing a scene through multiple, distinct \mathbf{S}_i matrices. However, prior works on leveraging multiple cameras [13, 14] do not tackle with unavoidable image misalignment.

Can we turn a multi-camera smartphone into a compact, spectrally diverse imaging system, without altering its internal hardware? Our key insight is that by modulating the spectral response of the auxiliary cameras using carefully chosen external filters, we can create a 9-channel imaging system from off-the-shelf devices. Unlike synthetic

MSFAs or custom hardware, our approach requires no internal modification and enables real-time, parallel acquisition. Critically, this setup is easy to deploy, manufacturable at scale, and compatible with existing mobile infrastructure.

We select filters using spectral information loss minimization with respect to a representative hyperspectral distribution. The resulting setup produces spatially misaligned but spectrally rich multi-view data thus posing a new fusion problem that we address via alignment-aware learning. An overview of our physical configuration is shown in Fig. 1, which illustrates how external filters are applied to the auxiliary lenses of a standard smartphone to create a spectrally diverse input set. The combination of low-cost physical augmentation and learning-based reconstruction represents a practical path toward deployable hyperspectral imaging in unconstrained environments. We propose a complete, low-cost pipeline for *multi-image-to-hyperspectral reconstruction (MI-HSR)* using a filter-modified smartphone. Specifically, the contributions are three-fold:

- A novel smartphone-based acquisition system that uses two custom spectral filters over auxiliary cameras, converting a consumer-grade smartphone into a 9-channel imaging device. We analyze and justify our filter choices via information-theoretic criteria. To the best of our knowledge, such a configuration has not been previously explored in HSR literature. Our system significantly outperforms RGB-only and naive multi-view baselines.
- The *Doomer* dataset, the first benchmark for MI-HSR. It contains 4 captures per scene: three from each of smartphone’s camera and the fourth from the hyperspectral camera.
- A principled reformulation of transformer-based HSR architecture for our setting, showing that spatial-first attention enables implicit alignment and effective fusion of misaligned inputs across camera viewpoints.

2 Related Work

Low-cost multispectral imaging. Numerous approaches have aimed to capture multispectral or hyperspectral information without expensive hardware. Early work by Helling et al. [15] employed a grayscale camera with a rotating filter wheel, while Valero et al. [16] used an RGB camera with three interchangeable filters. Oh et al. [14] captured scenes with three different cameras, leveraging the variation in their spectral sensitivities. More recently, Sharma et al. [13] demonstrated that consumer mobile devices with both RGB and NIR sensors can achieve extended spectral capture (400–1000 nm). Although these systems reduce costs, they either involve long capture times or assume no misalignment between successive captures.

Hyperspectral reconstruction from RGB. Traditional HSR methods model spectra using sparse coding [17], dictionary learning [18], or manifold embeddings [19], based on the low-dimensional structure of hyperspectral data and the rarity of metamers [20]. These approaches are computationally efficient but often lack the

capacity to incorporate global context from the input image, making them less robust to complex natural scenes. Recent methods based on deep learning have achieved significant advances, particularly those developed through the NTIRE spectral reconstruction challenges [21, 22, 23]. Early deep models used CNNs [9, 24, 25, 26, 27, 28], while newer transformer-based approaches like MST++ [8] and MSFN [29] introduced attention along spectral or spatial dimensions. However, nearly all research relies on synthetic RGB inputs rendered from hyperspectral images (HSIs) using color matching functions (CMFs), assuming perfect alignment and access to camera parameters. These assumptions do not hold in practice, limiting model generalizability. We address these limitations training and evaluating on real-world data with acquisition artifacts and misalignment.

Handling misalignment. Misalignment between inputs and ground truth is a well-known challenge in video and reference-based super-resolution tasks. Optical flow (OF) [30, 31], deformable convolutions [32, 33], and attention mechanisms [34] have been proposed to mitigate this. In our context, misalignment also arises due to ground truth HSIs being not spatially aligned with the RGB input. Zhang et al. [35] addressed this by warping ground truth toward the input using OF, enabling pixel-level evaluation. Elezabi et al. [36] proposed contextual losses and pseudo-aligned inputs as training strategies. We adopt the interpretable and evaluation-friendly approach [35] of warping the ground truth to the input using OF, allowing accurate pixel-wise supervision and metric computation.

Hyperspectral datasets. Several datasets support HSR research. Early datasets like CAVE [37] and Harvard [38] provided controlled hyperspectral measurements. Later datasets such as ICVL [17], KAUST [39], and ARAD_1K [23] focused on enabling data-driven HSR methods. These datasets contain either radiance or reflectance data, but most lack real RGB images and instead simulate RGB via CMFs, which fails to capture the characteristics of camera pipelines. Moreover, they often assume perfect alignment, which does not hold in practical settings. Recent datasets like BeyondRGB [5] and MobileSpec [4] address some of these issues by including real RGB captures. BeyondRGB includes color charts and lightsource spectrum estimation, while MobileSpec offers aligned RGB-HSI pairs. However, they still face trade-offs between alignment, diversity, and color reference availability. We build on these efforts by introducing Doomer dataset with real RGB images, misaligned hyperspectral data, and in-scene color references thus enabling realistic reconstruction under natural capture conditions.

3 Proposed Imaging System

3.1 System Overview

Our goal is to improve HSR by increasing the number of spectrally distinct measurements captured simultaneously, using only consumer-grade hardware. Rather than relying on custom sensor arrays or coded optics, we build upon multi-camera smartphones, which are already equipped with multiple rear-facing cameras featuring different lenses and spectral sensitivity functions (SSFs).

Dataset	# scenes	Spectral data	Color reference	Spectral sampling Range (step), nm	Corresponding RGBs
CAVE [37]	32	Reflectance	Color chart or no	400–700 (10)	simulated BMP
Harvard [38]	79	Radiance	No	400–720 (10)	No
ICVL [17]	200	Radiance	Color chart or no	400–1000 (10)	simulated JPEG
KAUST [39]	409	Reflectance	White patch	400–730 (10)	No
ARAD_1K [23]	950	Radiance	No	400–700 (10)	simulated JPEG
Beyond RGB [5]	1680	Radiance	Color chart	380–730 (20)	2× real RAW
MobileSpec [4]	200	Radiance	No	400–1000 (10)	real RAW
Doomer (proposed)	143	Radiance	Gray ball	400–730 (10)	3× real RAW

Table 1: Comparison of existing hyperspectral datasets. Our proposed Doomer dataset uniquely offers real multi-view RGB images with spectral filters, misalignment, and in-scene gray reference under diverse conditions.

To amplify spectral diversity, we augment the auxiliary cameras with external filters. As illustrated in Fig. 1, this converts each RGB camera into a spectrally modulated sensor. The resulting device captures nine distinct spectral channels: three from each RGB camera, modified by its filter without requiring scanning or internal hardware changes.

Formally, let $\mathbf{S}_i \in \mathbb{R}^{3 \times n}$ be the SSF of camera i , and $\mathbf{f}_i \in [0, 1]^n$ the spectral transmittance of the filter applied to that camera. The effective per-camera response becomes $\mathbf{S}_i \circ \mathbf{f}_i$, and the overall system response is:

$$\mathbf{S}_{\mathbf{F}} = \begin{bmatrix} \mathbf{S}_1 \circ \mathbf{f}_1 \\ \mathbf{S}_2 \circ \mathbf{f}_2 \\ \dots \\ \mathbf{S}_k \circ \mathbf{f}_k \end{bmatrix} \in \mathbb{R}^{3k \times n},$$

where $\mathbf{F} = [\mathbf{f}_1^\top; \dots; \mathbf{f}_k^\top]$ denotes the filter configuration. In our prototype, $k = 3$, with one unfiltered camera ($\mathbf{f}_1 = \mathbf{1}$) and two filtered cameras. This design simplifies dataset collection (Sec. 4) while still significantly expanding the observed spectral basis.

This configuration has two practical advantages. First, all channels are captured simultaneously under natural illumination, making it suitable for dynamic scenes. Second, it relies entirely on off-the-shelf hardware components. However, as each camera has a distinct physical position, the resulting images are spatially misaligned. This necessitates learning-based alignment modules, which we incorporate into our reconstruction pipeline (Sec. 5).

3.2 Filter Selection via Spectral Uncertainty Minimization

The effectiveness of our imaging system critically depends on the choice of spectral filters. Since we train on fully real-world data, the filter configuration must be fixed prior to data collection.

Given a library of $N = 65$ candidate filters available in our lab, we exhaustively evaluate all 65×64 ordered filter pairs for the two auxiliary cameras. The optimal

pair should minimize spectral ambiguity — i.e., the uncertainty in the latent spectrum $\mathbf{r} \in \mathbb{R}^n$ given a measurement $\mathbf{c} = \mathbf{S}_F \mathbf{r} + \mathbf{n}$, where \mathbf{n} is sensor noise.

Following [40], we use the expected conditional variance of the spectrum as our selection criterion:

$$v(\mathbf{F}) = \mathbb{E}_{\mathbf{c}} [\text{tr } \mathbb{V}_{\mathbf{r}}(\mathbf{r} \mid \mathbf{c})].$$

This criterion reflects the average spectral uncertainty remaining after observing \mathbf{c} . Lower $v(\mathbf{F})$ implies more informative measurements and improved reconstructibility.

To compute this metric, we sample spectra \mathbf{r} from a uniform distribution over pixels in a publicly available hyperspectral dataset [39] (licensed under CC BY-NC 3.0). We use precise SSFs for our smartphone cameras and spectrophotometer-measured filter transmittances (see Sec. A.1 for details). The final filter pair (Fig. 2) is selected as the one that minimizes $v(\mathbf{F})$.

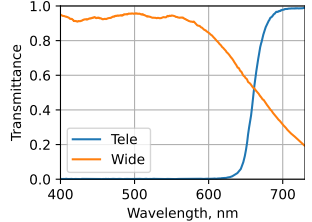


Figure 2: Filters selected for Tele and Wide cameras.

4 *Doomer* Dataset

Overview. To support training and evaluation for the MI-HSR task introduced in Section 3, we collect a new dataset, which we call *Doomer*¹. Existing hyperspectral datasets are not suited for our setup: none provide spatially misaligned multi-view RGB observations. Furthermore, no existing dataset aligns with our specific hardware configuration (a triple-camera smartphone with custom spectral filters), making new data collection a necessity.

Doomer contains 143 real-world scenes captured using a Huawei Mate 40 Pro smartphone equipped with Main, Tele, and Wide cameras, along with a Specim IQ hyperspectral camera for ground truth. In each scene, we record three smartphone RAW images, two with custom spectral filters and one unfiltered as well as a 111-band (400 – 730 nm) hyperspectral image. Example captures are shown in Figure 3.

Scenes include a mix of indoor and outdoor environments under varying illumination conditions (e.g., halogen and LED lighting indoors; overcast and sunny weather outdoors), and span a range of objects including food, printed material, architectural surfaces, and color calibration charts. Each scene includes a gray ball reference for future work on illumination estimation. While the gray ball is visible in Wide and Main cameras, it falls outside the Tele field of view and is cropped out during preprocessing. Non-processed versions will be included in the public release.

Gray ball reference makes the proposed dataset potentially useful in research on illumination estimation, automatic white balance and color space transform (see Sec. A.3 for more detailed proposals).

Capture setup. The data acquisition rig consists of a Specim IQ hyperspectral camera, a Huawei Mate 40 Pro smartphone mounted in a 3D-printed case with slots for spectral filters and a gray reference sphere (VFX ball).

¹The name *Doomer* is inspired by the subcultural aesthetic: most scenes were collected under gloomy or overcast weather conditions, in contrast to the brightly lit existing datasets.

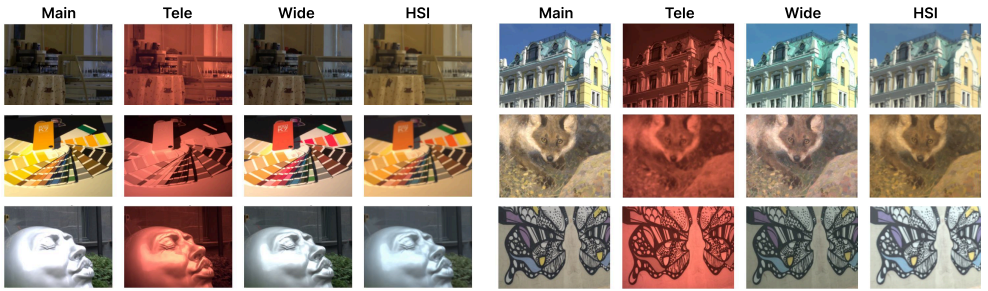


Figure 3: Sample scenes from the *Doomer* dataset. Smartphone images are rendered to sRGB using device-specific color matrices; hyperspectral images are rendered using CIE RGB CMF.

The entire system is mounted on a tripod, with the phone positioned to rotate along a vertical axis for alternating captures (Figure 4). This design allows the smartphone and hyperspectral camera to image scenes from nearly identical viewpoints, minimizing parallax and occlusion. The gray ball is connected to a rigid rod that allows to regulate the position of the ball in the scene.

Image acquisition proceeds sequentially: first, all three smartphone cameras capture RAW images; then, the smartphone case is moved to make hyperspectral image. Most smartphone settings (e.g., ISO, shutter speed) are controlled automatically, except in scenes with poor red signal where we manually adjusted Tele exposure to avoid excessive noise.

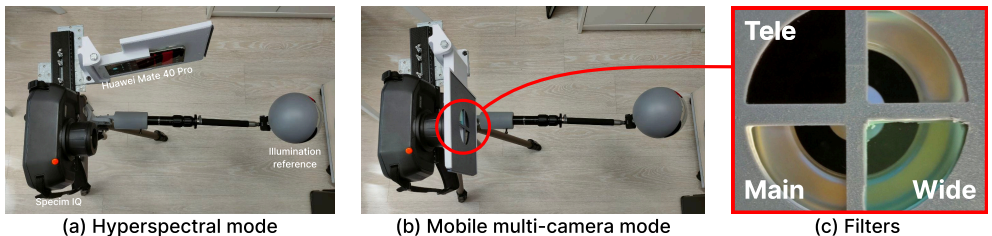


Figure 4: *Capture setup for the Doomer dataset.* (a) Smartphone holder rotated to allow hyperspectral capture via Specim IQ. (b) Smartphone repositioned for simultaneous multi-camera RGB capture. (c) External spectral filters mounted on Tele and Wide cameras to induce spectral diversity.

Preprocessing pipeline. Each four-image scene group (three RGB + one HSI) undergoes standardized preprocessing (see Supp.). We also normalize field of view and resolution across sensors. Specifically, we estimate pairwise homographies between each RGB image and the Tele view using SIFT keypoints and RANSAC. All images are then warped to the Tele frame and cropped accordingly (Fig. 5). When automatic registration fails, manual alignment is used. Despite this correction, residual geometric misalignment remains due to parallax and non-planar scene structure — motivating

our use of alignment-aware HSR models. Finally, all images are downsampled to match the hyperspectral resolution, originally 194×259 cropped to 192×256 for convenience, and spectral grid is resampled to conventional 400–730 nm, $n = 34$, to optimize computational costs.



Figure 5: *Spatial preprocessing pipeline.* Left: geometric alignment of RGB views using SIFT + RANSAC for consistent cross-camera registration. Right: field-of-view normalization and resolution matching across RGB and hyperspectral modalities.

5 Method

The task of MI-HSR involves predicting a hyperspectral image aligned to a target viewpoint (the Main camera), given RGB images from multiple spatially offset sensors:

$$\mathbf{I}_{\text{Main}}, \mathbf{I}_{\text{Tele}}, \mathbf{I}_{\text{Wide}} \in \mathbb{R}^{h \times w \times 3}.$$

This setup introduces two key challenges: (i) the input views are misaligned due to differing camera geometries, and (ii) the available hyperspectral supervision $\mathbf{I}_{\text{HS}} \in \mathbb{R}^{h \times w \times n}$ corresponds to a reference sensor not aligned with any RGB input. Our approach addresses both issues, one through pre-processing, the other through architectural design.

5.1 Supervision Warping via Learned Optical Flow

To leverage the hyperspectral reference image for training, we align it to the Main RGB view using learned OF. Since spectral and RGB images differ in modality, we first compute a color projection $\mathbf{C} \in \mathbb{R}^{n \times 3}$ to transform \mathbf{I}_{HS} into an RGB approximation:

$$\mathbf{C} := \underset{\mathbf{C}}{\operatorname{argmin}} \|\mathbf{I}_{\text{HS}}\mathbf{C} - \mathbf{I}_{\text{Main}}\|_2^2.$$

Given $\mathbf{I}_{\text{HS}}\mathbf{C}$ and \mathbf{I}_{Main} , we estimate a dense correspondence field $\boldsymbol{\delta} \in \mathbb{R}^{h \times w \times 2}$ using a pre-trained OF model \mathcal{F} (PWC-Net [41]):

$$\boldsymbol{\delta} := \mathcal{F}(\mathbf{I}_{\text{HS}}\mathbf{C}, \mathbf{I}_{\text{Main}}).$$

This flow is used to warp the hyperspectral GT to the Main view:

$$\mathbf{I}_{\text{HS}}^{\text{w}} := \mathcal{W}(\mathbf{I}_{\text{HS}}, \boldsymbol{\delta}), \quad \mathbf{m} := \lfloor \mathcal{W}(\mathbf{1}, \boldsymbol{\delta}) \rfloor,$$

where \mathbf{m} is a binary mask indicating valid visible pixels. This enables aligned supervision for training and pointwise loss computation $\mathcal{L}_1(\mathbf{I}_{\text{HS}}^{\text{w}} \circ \mathbf{m}, \hat{\mathbf{I}}_{\text{HS}} \circ \mathbf{m})$

5.2 Implicit Cross-View Alignment in Network Design

Even with warped supervision, the three input views remain spatially misaligned. Direct calibration or flow-based alignment is possible but impractical in general-purpose settings. Instead, we encode alignment into the architecture itself, drawing inspiration from recent findings that transformer attention can perform implicit alignment across modest viewpoint shifts [42].

We adopt MSFN [29] as our base model, which consists of spatial and spectral transformer-based U-Nets. However, its original design applies spectral modeling before spatial, which is unsuitable for misaligned inputs as spectral attention assumes spatial coherence across input channels, which multi-camera setups violate.

5.3 Proposed Architecture: MI-MSFN

We propose a revised architecture, Multi-Image MSFN (MI-MSFN), specifically tailored to address input misalignment and heterogeneous spatial content. Here, we reverse the order of modules, applying spatial transformer blocks before spectral ones (Figure 6). This allows the network to first establish spatial correspondences across the Main, Tele, and Wide inputs thus effectively aligning features by attention before fusing spectral information. We also remove the skip paths to enforce that all feature propagation passes through alignment-aware components.

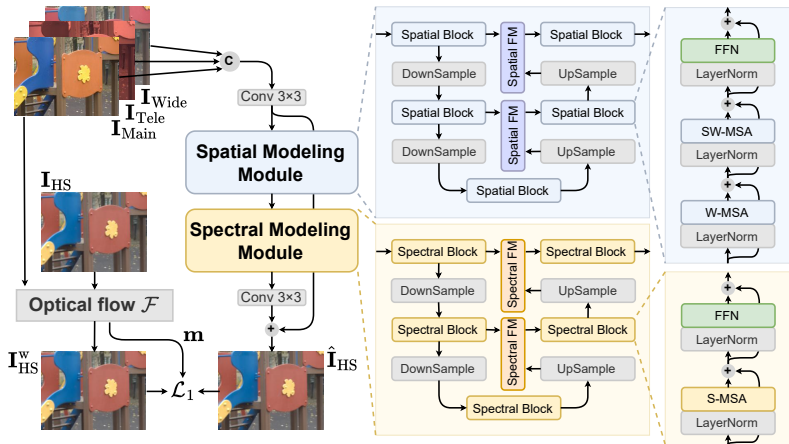


Figure 6: Overview of the proposed MI-MSFN architecture for multi-image hyperspectral reconstruction. It integrates implicit alignment across misaligned inputs via spatial-first attention, followed by spectral modeling. For detailed module definitions (*Spectral FM*, *Spatial FM*), refer to Sec. A.4

6 Experiments

6.1 Experimental Setup

Dataset. All the experiments were conducted on our *Doomer* dataset as it is the only available one for MI-HSR task. Experiments on single-image HSR were only conducted for comparison to MI-HSR, thus featuring the same dataset.

Metrics. We adopt well-known Peak Signal-to-Noise Ratio (PSNR) and Spectral Angle Mapper (SAM). We also introduce Normalized Spectral Error (NSE), which serves as an alternative to MRAE as it does not penalize having few dark bands and reflects the integral nature of radiance:

$$\text{NSE}(\hat{\mathbf{r}}, \mathbf{r}) = \frac{\|\hat{\mathbf{r}} - \mathbf{r}\|_1}{\|\mathbf{r}\|_1} \cdot 100\%, \quad \mathbf{r}, \hat{\mathbf{r}} \in \mathbb{R}^n.$$

When comparing predictions to warped GT, some pixels were missing or invalid, so we masked out positions at $\mathbf{m}(x, y) = 0$.

Implementation details. We split our dataset into *train* and *test* subset in proportion 4:1. In all the experiments we used Adam optimizer with learning rate of 0.0004 inherited MSFN (except for AWAN at Sec. 6.3, which showcased the necessity of polynomial scheduler with power of 1.5 starting at learning rate of 0.0001). We trained all the networks on random 64×64 patches for 10^4 epochs. Every 30 epochs we ran evaluation loop; the final model is the one with the best mean absolute error on the aligned test set. Each training procedure was re-run 10 times with different random seeds, yielding 10 distinct quantitative results. We summarize them by reporting mean and standard deviation.

6.2 Results

We trained the proposed MI-MSFN network using two input configurations: single-image (\mathbf{I}_{Main}) and multi-image ($\mathbf{I}_{\text{Main}}, \mathbf{I}_{\text{Tele}}, \mathbf{I}_{\text{Wide}}$). To validate our supervision alignment (Sec. 5), following [35], we report metrics both on aligned and original GT in Tab. 2. Our multi-image acquisition system improves HSR by 3.56 dB PSNR, 38% SAM, 28% NSE. The lower standard deviation (1–3% of mean value) underlines the learning stability of the proposed MI-MSFN approach.

Setting	Aligned GT			Original GT		
	PSNR, dB \uparrow	SAM, $^\circ$ \downarrow	NSE, % \downarrow	PSNR, dB \uparrow	SAM, $^\circ$ \downarrow	NSE, % \downarrow
Single-camera	26.30 \pm 0.68	6.11 \pm 0.40	12.71 \pm 0.46	25.05 \pm 0.48	6.25 \pm 0.42	14.14 \pm 0.67
Multi-camera	29.86 \pm 0.21	3.77 \pm 0.09	9.14 \pm 0.20	27.88 \pm 0.15	3.91 \pm 0.08	10.35 \pm 0.16

Table 2: Evaluations of MI-MSFN in single- and multi-camera settings. Mean and standard deviation of each metric is computed across 10 re-runs. The use of auxiliary cameras allows highly better HSR.

Fig. 7 presents a qualitative comparison between single-camera and multi-camera configurations. We show patch-level comparisons at a selected wavelength as well as radiance profiles at specific points of interest. The multi-camera system consistently

recovers finer surface details that the single-camera setup fails to capture. In the first row, a printed symbol on a book cover is not registered by the multi-camera system at $\lambda = 700$ nm which complies with GT while SI-HSR falsely reveals the symbol. In the second row, the single-camera system introduces spurious noise-like structures that do not correspond to any physical features. In the third row, the single-image setup fails to reconstruct radiometric intensity accurately, significantly misestimating the radiance of the paper sheet. We also showcase a failure case of our system in the fourth row. These results highlight the improved spatial and spectral fidelity enabled by multi-view fusion in the MI-HSR system.

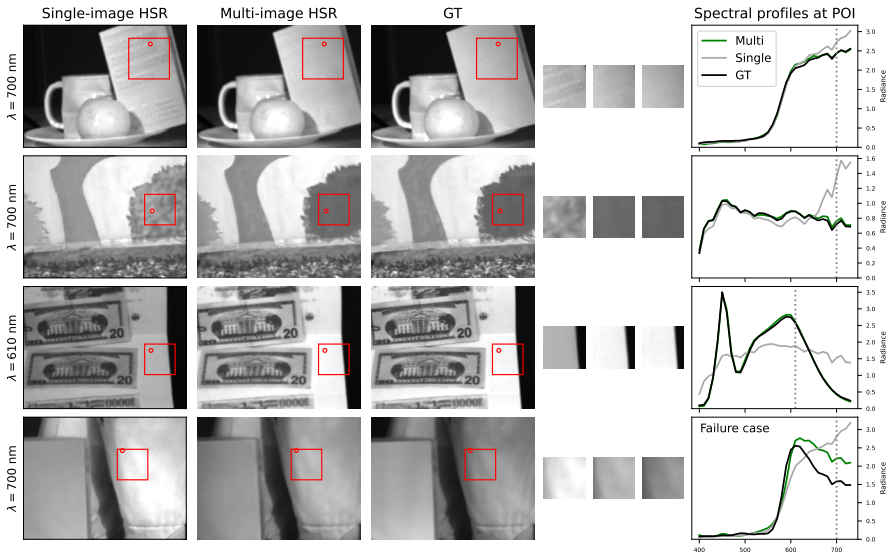


Figure 7: Qualitative comparison of MI-MSFN predictions under single-image and multi-image input settings. For each scene, a specific spectral band, region of interest, and point of interest are selected. Regions are enlarged and displayed side-by-side to highlight differences in spatial and spectral reconstruction quality. Note that the grayscale renderings correspond to individual spectral bands, as shown at the wavelength indicated on the left of each image.

6.3 Ablation Study

We conducted two ablation studies, beginning with replacement of HSR network. We compared MI-MSFN against several approaches: HSCNN+ [24], AWAN [22, 43], MST++ [8] (winners of NTIRE 2018 [21], 2020 [22], 2022 [23] respectively) and MSFN [29] as shown in Tab. 3. Since we evaluate them in our misaligned multi-image setting they were not designed for, we also help them by warping inputs onto the Main camera view using the same pre-trained OF as before. In particular, Tab. 3 depicts the superiority of MI-MSFN over MSFN, justifying the proposed architectural changes.

The second ablation study evaluates contribution of each auxiliary camera. It

Method	OF	PSNR, dB \uparrow	SAM, $^\circ$ \downarrow	NSE, % \downarrow
HSCNN+ [24]	-	26.28 \pm 0.40	5.66 \pm 0.13	12.20 \pm 0.13
	\checkmark	26.46 \pm 0.64	5.76 \pm 0.13	12.23 \pm 0.17
AWAN [43]	-	27.01 \pm 0.79	4.56 \pm 0.08	10.80 \pm 0.10
	\checkmark	26.41 \pm 1.30	4.49 \pm 0.17	10.68 \pm 0.20
MST++ [8]	-	29.01 \pm 0.25	4.18 \pm 0.15	9.86 \pm 0.17
	\checkmark	29.37 \pm 0.31	4.11 \pm 0.07	9.66 \pm 0.11
MSFN [29]	-	29.18 \pm 0.21	3.91 \pm 0.13	9.77 \pm 0.13
	\checkmark	29.59 \pm 0.21	3.93 \pm 0.13	9.33 \pm 0.23
MI-MSFN (ours)	-	29.86 \pm 0.21	3.77 \pm 0.09	9.14 \pm 0.20

Table 3: Ablation study on HSR model showing MI-MSFN being the best choice for MI-HSR.

extends Tab. 2 by two more settings: ($\mathbf{I}_{\text{Main}}, \mathbf{I}_{\text{Tele}}$) and ($\mathbf{I}_{\text{Main}}, \mathbf{I}_{\text{Wide}}$). Results are given in Tab. 4. We can see that just by adding the Tele-camera we are already close to the performance of all three. Notably, this camera was occluded by the red filter (Fig. 2) and most examples from qualitative comparison (Fig. 7) showcase how our setup handles discrepancy in red spectral range. In terms of NSE-metric, the combination of Main and Tele even outperforms everything, but statistically insignificantly.

6.4 Effect of Noise in Hyperspectral Camera

Hyperspectral image registration is a process of registering photons, which means our GTs are inherently noisy just like consumer CMOS sensors. Since noise is unpredictable, HSR quality has a physically-reasoned insurmountable boundary. To quantify this boundary, we captured series of HSIs of static scenes with color charts under two different light conditions. The metrics were calculated between a fixed image from a series and the average of remain images, see Tab. 5. The estimated values should be interpreted as approximate bound for any MI-MSR network trained and tested on Doomer dataset. Comparable metric values may indicate overfitting or sensitivity to sensor noise.

Light conditions	PSNR, dB \uparrow	SAM, $^\circ$ \downarrow	NSE, % \downarrow
Bright scenario (outdoor sunny)	41.32 \pm 3.04	0.71 \pm 0.11	3.13 \pm 0.55
Medium brightness (indoor LED)	37.81 \pm 3.49	1.02 \pm 0.12	4.46 \pm 1.27

Table 5: Metrics measured between several Specim IQ shots of the same scene. These values suggest rough estimates of the highest probable quality of HSR on Doomer.

7 Limitations

The trained models in this work are tightly coupled to the spectral characteristics and quantum efficiency of the specific RGB sensors and optical filters used in our acquisition setup. As a result, deploying the system with different hardware configurations would require collecting a new dataset and retraining the model. This limits immediate out-of-the-box generalization. Future research could explore strategies such as sensor-specific domain adaptation, transfer learning, or SSF-invariant reconstruction frameworks to improve reproducibility and portability across different camera systems.

Active cameras				PSNR, dB \uparrow	SAM, $^\circ$ \downarrow	NSE, % \downarrow
Main	Tele	Wide				
\checkmark				26.30 \pm 0.68	6.11 \pm 0.40	12.71 \pm 0.46
\checkmark		\checkmark		26.34 \pm 0.67	5.77 \pm 0.31	12.41 \pm 0.46
\checkmark	\checkmark			29.63 \pm 0.28	3.97 \pm 0.11	9.08 \pm 0.33
\checkmark	\checkmark	\checkmark		29.86 \pm 0.21	3.77 \pm 0.09	9.14 \pm 0.20

Table 4: Ablation study on cameras configuration. Each camera brings an improvement in SAM.

8 Conclusion

This work rethinks HSR through the lens of practical acquisition. By moving beyond single RGB image constraints, we demonstrate that leveraging multiple smartphone cameras with carefully chosen spectral filters can significantly enrich the input signal and reduce ambiguity in reconstruction. Our proposed MI-HSR framework shows that spectral diversity even when captured with commodity hardware can close the gap between simulated and real-world hyperspectral imaging. The introduction of the Doomer dataset marks an important step forward for benchmarking in this space, enabling systematic evaluation of multi-view HSR under realistic conditions. Empirical results validate both our hardware configuration and model design, suggesting a promising direction for low-cost, deployable hyperspectral imaging systems. Looking ahead, we aim to further explore the temporal dimension for dynamic scenes, optimize for energy-efficient mobile deployment, and investigate more principled learning paradigms under limited supervision or device mismatch.

References

- [1] Xiang Xu, Jun Li, Xin Huang, Mauro Dalla Mura, and Antonio Plaza. Multiple morphological component analysis based decomposition for remote sensing image classification. *IEEE Transactions on Geoscience and Remote Sensing*, 54(5):3083–3102, 2016.
- [2] Meiling Wang, Yongchang Xu, Zhisheng Wang, and Changda Xing. Deep margin cosine autoencoder-based medical hyperspectral image classification for tumor diagnosis. *IEEE Transactions on Instrumentation and Measurement*, 72:1–12, 2023.
- [3] Seon Joo Kim, Fanbo Deng, and Michael S Brown. Visual enhancement of old documents with hyperspectral imaging. *Pattern Recognition*, 44(7):1461–1469, 2011.
- [4] Kailai Zhou, Lijing Cai, Yibo Wang, Mengya Zhang, Bihan Wen, Qiu Shen, and Xun Cao. Joint rgb-spectral decomposition model guided image enhancement in mobile photography. In *Proceedings of the IEEE/CVF European Conference on Computer Vision*. Springer, 2024.
- [5] Ortal Glatt, Yotam Ater, Woo-Shik Kim, Shira Werman, Oded Berby, Yael Zini, Shay Zelinger, Sangyoon Lee, Heejin Choi, and Evgeny Soloveichik. Beyond rgb: a real world dataset for multispectral imaging in mobile devices. In *Proceedings of the IEEE/CVF Winter Conference on Applications of Computer Vision*, 2024.
- [6] Da-Wen Sun, Hongbin Pu, and Jingxiao Yu. Applications of hyperspectral imaging technology in the food industry. *Nature Reviews Electrical Engineering*, 1(4):251–263, 2024.
- [7] Md Toukir Ahmed, Ocean Monjur, and Mohammed Kamruzzaman. Deep learning-based hyperspectral image reconstruction for quality assessment of agro-product. *Journal of Food Engineering*, 382:112223, 2024.
- [8] Yuanhao Cai, Jing Lin, Zudi Lin, Haoqian Wang, Yulun Zhang, Hanspeter Pfister, Radu Timofte, and Luc Van Gool. Mst++: Multi-stage spectral-wise transformer for efficient spectral reconstruction. In *Proceedings of the IEEE/CVF Conference on Computer Vision and Pattern Recognition*, 2022.

- [9] Yuzhi Zhao, Lai-Man Po, Qiong Yan, Wei Liu, and Tingyu Lin. Hierarchical regression network for spectral reconstruction from rgb images. In *Proceedings of the IEEE/CVF Conference on Computer Vision and Pattern Recognition Workshops*, 2020.
- [10] Renjie Wu, Yuqi Li, Xijiong Xie, and Zhijie Lin. Optimized multi-spectral filter arrays for spectral reconstruction. *Sensors*, 19(13):2905, 2019.
- [11] Shijie Nie, Lin Gu, Yinqiang Zheng, Antony Lam, Nobutaka Ono, and Imari Sato. Deeply learned filter response functions for hyperspectral reconstruction. In *Proceedings of the IEEE/CVF Conference on Computer Vision and Pattern Recognition*, 2018.
- [12] Ying Fu, Tao Zhang, Yinqiang Zheng, Debing Zhang, and Hua Huang. Joint camera spectral sensitivity selection and hyperspectral image recovery. In *Proceedings of the IEEE/CVF the European Conference on Computer Vision*, 2018.
- [13] Neha Sharma, Muhammad Shahzaib Waseem, Shahrzad Mirzaei, and Mohamed Hefeeda. Mobispectral: Hyperspectral imaging on mobile devices. In *Proceedings of the 29th Annual International Conference on Mobile Computing and Networking*, 2023.
- [14] Seoung Wug Oh, Michael S Brown, Marc Pollefeys, and Seon Joo Kim. Do it yourself hyperspectral imaging with everyday digital cameras. In *Proceedings of the IEEE/CVF Conference on Computer Vision and Pattern Recognition*, 2016.
- [15] Stephan Helling, Enrico Seidel, and Wolfram Biehlig. Algorithms for spectral color stimulus reconstruction with a seven-channel multispectral camera. In *Conference on Colour in Graphics, Imaging, and Vision*. Society of Imaging Science and Technology, 2004.
- [16] Eva M Valero, Juan L Nieves, Sergio MC Nascimento, Kinjiro Amano, and David H Foster. Recovering spectral data from natural scenes with an rgb digital camera and colored filters. *Color Research & Application*, 32(5):352–360, 2007.
- [17] Boaz Arad and Ohad Ben-Shahar. Sparse recovery of hyperspectral signal from natural rgb images. In *Proceedings of the IEEE/CVF the European Conference on Computer Vision*, 2016.
- [18] Jonas Aeschbacher, Jiqing Wu, and Radu Timofte. In defense of shallow learned spectral reconstruction from rgb images. In *Proceedings of the IEEE/CVF International Conference on Computer Vision Workshops*, 2017.
- [19] Yan Jia, Yinqiang Zheng, Lin Gu, Art Subpa-Asa, Antony Lam, Yoichi Sato, and Imari Sato. From rgb to spectrum for natural scenes via manifold-based mapping. In *Proceedings of the IEEE/CVF International Conference on Computer Vision*, 2017.
- [20] David H Foster, Kinjiro Amano, Sérgio MC Nascimento, and Michael J Foster. Frequency of metamerism in natural scenes. *Journal of the Optical Society of America A*, 23(10):2359–2372, 2006.
- [21] Boaz Arad, Dong Liu, Feng Wu, Charis Lanaras, Silvano Galliani, Konrad Schindler, Tarek Stiebel, Simon Koppers, Philipp Seltsam, Ruofan Zhou, Majed El Helou, Ohad Ben-Shahar, Fayez Lahoud, Marjan Shahpaski, Ke Zheng, Lianru Gao, Bing Zhang, Ximin Cui, Haoyang Yu, Yigit Baran Can, Aitor Alvarez-Gila, Joost van de Weijer, Radu Timofte, Estibaliz Garrote, Adrian Galdran, Manoj Sharma, Sriharsha Koundinya, Avinash Upadhyay, Raunak Manekar, Rudrabha Mukhopadhyay, Himanshu Sharma, Santanu Chaudhury, Koushik Nagasubramanian, Luc Van Gool, Sambuddha Ghosal, Asheesh K. Singh, Arti Singh, Baskar Ganapathysubramanian, Soumik Sarkar, Lei Zhang, Ming-Hsuan Yang, Zhiwei Xiong, Chang Chen, and Zhan Shi. Ntire 2018 challenge on

- spectral reconstruction from rgb images. In *Proceedings of the IEEE/CVF Conference on Computer Vision and Pattern Recognition Workshops*, 2018.
- [22] Boaz Arad, Radu Timofte, Ohad Ben-Shahar, Yi-Tun Lin, and Graham D Finlayson. Ntire 2020 challenge on spectral reconstruction from an rgb image. In *Proceedings of the IEEE/CVF Conference on Computer Vision and Pattern Recognition Workshops*, 2020.
- [23] Boaz Arad, Radu Timofte, Rony Yahel, Nimrod Morag, Amir Bernat, Yuanhao Cai, Jing Lin, Zudi Lin, Haoqian Wang, Yulun Zhang, et al. Ntire 2022 spectral recovery challenge and data set. In *Proceedings of the IEEE/CVF Conference on Computer Vision and Pattern Recognition*, 2022.
- [24] Zhan Shi, Chang Chen, Zhiwei Xiong, Dong Liu, and Feng Wu. Hscnn+: Advanced cnn-based hyperspectral recovery from rgb images. In *Proceedings of the IEEE/CVF Conference on Computer Vision and Pattern Recognition Workshops*, 2018.
- [25] Zhiwei Xiong, Zhan Shi, Huiqun Li, Lizhi Wang, Dong Liu, and Feng Wu. Hscnn: Cnn-based hyperspectral image recovery from spectrally undersampled projections. In *Proceedings of the IEEE/CVF International Conference on Computer Vision Workshops*, 2017.
- [26] Lei Zhang, Zhiqiang Lang, Peng Wang, Wei Wei, Shengcai Liao, Ling Shao, and Yanning Zhang. Pixel-aware deep function-mixture network for spectral super-resolution. In *Proceedings of the AAAI Conference on Artificial Intelligence*, volume 34, pages 12821–12828, 2020.
- [27] Tarek Stiebel, Simon Koppers, Philipp Seltsam, and Dorit Merhof. Reconstructing spectral images from rgb-images using a convolutional neural network. In *Proceedings of the IEEE/CVF Conference on Computer Vision and Pattern Recognition Workshops*, 2018.
- [28] Silvano Galliani, Charis Lanaras, Dimitrios Marmanis, Emmanuel Baltsavias, and Konrad Schindler. Learned spectral super-resolution. *arXiv preprint arXiv:1703.09470*, 2017.
- [29] Yaohang Wu, Renwei Dian, and Shutao Li. Multistage spatial–spectral fusion network for spectral super-resolution. *IEEE Transactions on Neural Networks and Learning Systems*, pages 1–11, 2024.
- [30] Tae Hyun Kim, Mehdi SM Sajjadi, Michael Hirsch, and Bernhard Scholkopf. Spatio-temporal transformer network for video restoration. In *Proceedings of the IEEE/CVF European Conference on Computer Vision*, 2018.
- [31] Kelvin CK Chan, Xintao Wang, Ke Yu, Chao Dong, and Chen Change Loy. Basicvsr: The search for essential components in video super-resolution and beyond. In *Proceedings of the IEEE/CVF Conference on Computer Vision and Pattern Recognition*, 2021.
- [32] Yapeng Tian, Yulun Zhang, Yun Fu, and Chenliang Xu. Tdan: Temporally-deformable alignment network for video super-resolution. In *Proceedings of the IEEE/CVF Conference on Computer Vision and Pattern Recognition*, 2020.
- [33] Xintao Wang, Kelvin CK Chan, Ke Yu, Chao Dong, and Chen Change Loy. Edvr: Video restoration with enhanced deformable convolutional networks. In *Proceedings of the IEEE/CVF Conference on Computer Vision and Pattern Recognition Workshops*, pages 0–0, 2019.
- [34] Tengfei Wang, Jiaxin Xie, Wenxiu Sun, Qiong Yan, and Qifeng Chen. Dual-camera super-resolution with aligned attention modules. In *Proceedings of the IEEE/CVF International Conference on Computer Vision*, 2021.

- [35] Zhilu Zhang, Haolin Wang, Ming Liu, Ruohao Wang, Jiawei Zhang, and Wangmeng Zuo. Learning raw-to-srgb mappings with inaccurately aligned supervision. In *Proceedings of the IEEE/CVF International Conference on Computer Vision*, 2021.
- [36] Omar Elezabi, Zongwei Wu, and Radu Timofte. Enhanced super-resolution training via mimicked alignment for real-world scenes. In *Proceedings of the Asian Conference on Computer Vision*, 2024.
- [37] Fumihito Yasuma, Tomoo Mitsunaga, Daisuke Iso, and Shree K Nayar. Generalized assorted pixel camera: postcapture control of resolution, dynamic range, and spectrum. *IEEE transactions on image processing*, 19(9):2241–2253, 2010.
- [38] Ayan Chakrabarti and Todd Zickler. Statistics of real-world hyperspectral images. In *Proceedings of the IEEE/CVF Winter Conference on Applications of Computer Vision*, 2011.
- [39] Yuqi Li, Qiang Fu, and Wolfgang Heidrich. Multispectral illumination estimation using deep unrolling network. In *Proceedings of the IEEE/CVF International Conference on Computer Vision*, 2021.
- [40] Daniil Reutskii and Egor Ershov. Spectral filters design for a better hyperspectral reconstruction. In *Sixteenth International Conference on Machine Vision (ICMV 2023)*. SPIE, 2024.
- [41] Deqing Sun, Xiaodong Yang, Ming-Yu Liu, and Jan Kautz. Pwc-net: Cnns for optical flow using pyramid, warping, and cost volume. In *Proceedings of the IEEE/CVF Conference on Computer Vision and Pattern Recognition*, 2018.
- [42] Shuwei Shi, Jinjin Gu, Liangbin Xie, Xintao Wang, Yuju Yang, and Chao Dong. Rethinking alignment in video super-resolution transformers. *Advances in Neural Information Processing Systems*, 35:36081–36093, 2022.
- [43] Jiaojiao Li, Chaoxiong Wu, Rui Song, Yunsong Li, and Fei Liu. Adaptive weighted attention network with camera spectral sensitivity prior for spectral reconstruction from rgb images. In *Proceedings of the IEEE/CVF Conference on Computer Vision and Pattern Recognition Workshops*, 2020.
- [44] Alessandro Foi, Mejdj Trimeche, Vladimir Katkovnik, and Karen Egiazarian. Practical poissonian-gaussian noise modeling and fitting for single-image raw-data. *IEEE transactions on image processing*, 17(10):1737–1754, 2008.
- [45] Egor Ershov, Vasily Tesalin, Ivan Ermakov, and Michael S Brown. Physically-plausible illumination distribution estimation. In *Proceedings of the IEEE/CVF International Conference on Computer Vision*, 2023.
- [46] Ze Liu, Yutong Lin, Yue Cao, Han Hu, Yixuan Wei, Zheng Zhang, Stephen Lin, and Baining Guo. Swin transformer: Hierarchical vision transformer using shifted windows. In *Proceedings of the IEEE/CVF international conference on computer vision*, pages 10012–10022, 2021.
- [47] Alexey Dosovitskiy, Lucas Beyer, Alexander Kolesnikov, Dirk Weissenborn, Xiaohua Zhai, Thomas Unterthiner, Mostafa Dehghani, Matthias Minderer, Georg Heigold, Sylvain Gelly, et al. An image is worth 16x16 words: Transformers for image recognition at scale. *arXiv preprint arXiv:2010.11929*, 2020.

A Technical Appendices and Supplementary Material

To ensure disambiguation, here is the list of some designations used throughout the main paper and this document:

- Photometric normalization — division of a camera sensor signal by ISO (if applicable) and exposure time. Black current subtraction is also applied beforehand.
- \mathbf{c} — a photometrically normalized signal (probably noisy) from smartphone camera(s). Can be $\in \mathbb{R}^3$ or $\in \mathbb{R}^{3k}$ depending on context.
- $\bar{\mathbf{c}}$ — a photometrically normalized signal as it would be in an ideal world without noise.
- \mathbf{r} — a photometrically normalized radiance spectrum. Is assumed to be noiseless (however, in Sec. 6.4 of the main paper we discuss the outcomes of this assumption).
- \mathbf{x}_i — a vector from a set of vectors $\{\mathbf{x}_1, \mathbf{x}_2, \dots\}$
- x_i — i -th component of \mathbf{x} .

A.1 Estimation of Spectral Sensitivity Functions and Transmittance Functions

Spectral sensitivity functions. To estimate SSF of a smartphone camera, we acquired 25 sample pairs of $\mathbf{c}_i \in \mathbb{R}^3$ and $\mathbf{r}_i \in \mathbb{R}^n$ corresponding to flat-field illumination (FFI) of narrow-band LED light sources in an integrating sphere. For each LED i , we took a photo of FFI (Fig. 8), extracted the central 100×100 patch from it, photometrically normalized it and computed the channel-wise average to get \mathbf{c}_i . Then we measured the LED radiance spectrum \mathbf{r}_i using an X-Rite i1 Pro spectrophotometer with the help of `spotread` routine from Argyll color management system.

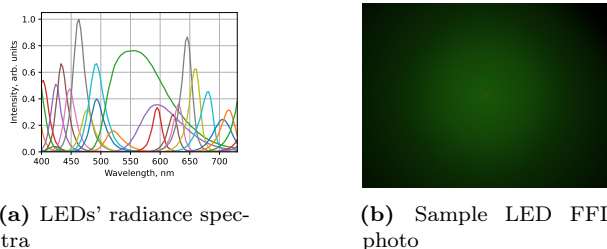
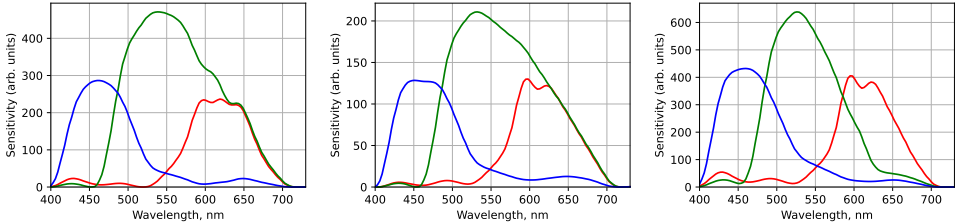


Figure 8: Training data for SSF estimation: (a) spectra of 25 LEDs measured using X-Rite i1 Pro; (b) an example of raw FFI photo. Notice the vignetting effect. To mitigate this effect, channel-wise average of a tiny central patch (in red) was used as a sample \mathbf{c}_i

Given the measurements $\{\mathbf{c}_i, \mathbf{r}_i\}_{i=1}^{25}$, the spectral sensitivities estimation problem can be formulated as a regularized quadratic optimization problem:

$$\begin{aligned} \min_{\mathbf{S}} \quad & \sum_{i=1}^{25} \|\mathbf{c}_i - \mathbf{S}^\top \mathbf{r}_i\|_2^2 + \lambda \|\mathbf{DS}\|_2^2 \\ \text{s. t.} \quad & \mathbf{S} \geq 0 \end{aligned} \quad (1)$$

where the regularization term $\lambda \|\mathbf{DS}\|_2^2$ imposes smoothness, \mathbf{D} is the second-order derivative operator. The objective (1) was minimized using the Adam optimizer.



(a) Main camera sensitivities (b) Tele camera sensitivities (c) Wide camera sensitivities

Figure 9: Estimated smartphone cameras spectral sensitivities.

To validate the estimated $\hat{\mathbf{S}}$, we captured a color rendition chart by the Specim IQ hyperspectral camera and all three smartphone cameras. The HSI was calibrated (more on that in the next paragraph) and projected onto each camera’s sensor space to yield RGB predictions. We compared the predicted and actual RGBs of the color patches: pixels of a patch were pixel-wise averaged (Fig. 12 gives a sight on how such patches look like). The average angular error of color reproduction was $\approx 1^\circ$ — indistinguishable to a human eye.

Specim IQ calibration. Spectral measurements of X-Rite i1 Pro and Specim IQ are actually inconsistent. It is not surprising: Specim IQ is not designed to be photometrically accurate. Instead, it allows to estimate band-wise relations between the *calibration target* in a scene and other objects. However, if we estimate the band-wise calibration divisor between X-Rite i1 Pro and Specim IQ, we can further use it to obtain physically-correct HSIs. We illuminated the integration sphere using a mixture of LEDs that yields even spectral power distribution, obtained X-Rite and Specim IQ measurements of it and divided one by another:

$$\mathbf{k} = \mathbf{r}_{\text{specim}} \oslash \mathbf{r}_{\text{xrite}},$$

The divisor is applied to every HSI filmed by the Specim IQ in this research.

Since the operational range of Specim IQ is 400–1000 nm and the one of X-Rite is 380–730 nm, all our spectral measurements are defined on their intersection: 400–730 nm.

Transmittance functions of filters were measured using an SF-2000 spectrophotometer.

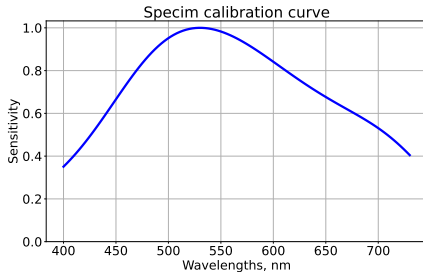


Figure 10: The estimated Specim IQ calibration divisor

A.2 Spectral Uncertainty

The inspiration comes from the well-known conditional entropy $H(\xi | \eta)$, which quantifies the information loss of a latent random variable ξ when observing the outcomes of another random variable η :

$$H(\xi | \eta) = \mathbb{E}_{x \sim \eta} H(\xi | \eta = x), \quad (2)$$

where $H(\xi | \eta = x)$ is the ordinary entropy of ξ given event $\eta = x$. However, entropy is designed especially for discrete-distributed variables of categorical type. When uncertainty of a categorical random variable is indeed best described by the entropy of its distribution, for continuous random variables variance is a better choice. When dealing with random vectors, variance becomes a matrix, so we consider the trace of it as a reasonable summary. If we put the trace of variance instead of the entropy in (2) and substitute $\xi = \mathbf{r}, \eta = \mathbf{c}$, we get the spectral uncertainty of our filters-modified optical system:

$$v(\mathbf{F}) = \mathbb{E}_{\mathbf{c}} [\text{tr } \mathbb{V}_{\mathbf{r}}(\mathbf{r} | \mathbf{c})],$$

where the dependence on \mathbf{F} is hidden inside the relationship between \mathbf{r} and \mathbf{c} . However, \mathbf{r} and \mathbf{c} are not random variables until we define them so. Let \mathbf{r} have a discrete distribution $p(\mathbf{r}_i)$ over a finite set of radiance spectra $\mathcal{R} = \{\mathbf{r}_1, \dots, \mathbf{r}_N\}$ derived from a dataset of HSIs. Such definition reflects the *a priori* information about natural radiance. In the relation $\mathbf{c} = \mathbf{S}_{\mathbf{F}}\mathbf{r} + \mathbf{n}$ only noise \mathbf{n} is yet to define. Let $\bar{\mathbf{c}} = \mathbf{S}_{\mathbf{F}}\mathbf{r}$ be an unnoised camera response. We model noise as

$$\mathbf{n} | \bar{\mathbf{c}} \sim \mathcal{N}(\mathbf{0}, \Sigma(\bar{\mathbf{c}})), \quad (3)$$

$$\Sigma(\bar{\mathbf{c}}) = \text{diag}[\sigma_1^2(\bar{c}_1); \dots; \sigma_{3k}^2(\bar{c}_{3k})], \quad (4)$$

where $\sigma_i(\cdot)$ is expanded in (5) later in the chapter.

Now, when we defined $p(\mathbf{c} | \mathbf{r})$, we can derive from the Bayesian rule:

$$p(\mathbf{r}_i | \mathbf{c}) = \frac{p(\mathbf{c} | \mathbf{r}_i) p(\mathbf{r}_i)}{\sum_{i=1}^N p(\mathbf{c} | \mathbf{r}_i) p(\mathbf{r}_i)},$$

and further:

$$\mathbb{E}_{\mathbf{r}}(\mathbf{r} \mid \mathbf{c}) = \sum_{i=1}^N p(\mathbf{r}_i \mid \mathbf{c}) \mathbf{r}_i,$$

$$\text{tr } \mathbb{V}_{\mathbf{r}}(\mathbf{r} \mid \mathbf{c}) = \sum_{i=1}^N p(\mathbf{r}_i \mid \mathbf{c}) \|\mathbf{r}_i - \mathbb{E}_{\mathbf{r}}(\mathbf{r} \mid \mathbf{c})\|_2^2.$$

Now we have an expression depending on \mathbf{c} which we should take $\mathbb{E}_{\mathbf{c}}$ of. However, this is intractable. So we should resort to Monte Carlo method by sampling \mathbf{c} according to its definition: first take random $\mathbf{r}^* \in \mathcal{R}$, then sample \mathbf{c} from $\mathcal{N}(\mathbf{S}_{\mathbf{F}}\mathbf{r}^*, \Sigma(\mathbf{S}_{\mathbf{F}}\mathbf{r}^*))$. In our experiments, 2^{20} samples were sufficient to achieve 0.5% of relative standard deviation.

To derive \mathcal{R} , we first extracted every 29×29 th pixel of the KAUST dataset [39], which resulted in 559,921 samples. However, this is a dataset of reflectances, so we converted them to radiance spectra via multiplying it by a spectrum of gray ball under overcast weather condition. This way, we assured that \mathcal{R} mostly fairly represents our future *Doomer* dataset. To reduce computational requirements, we also compressed \mathcal{R} to the size of $N = 1024$ by running K-Means algorithm and employing clusters' centers. We assigned $p(\mathbf{r}_i)$ to be the share of initial 559,921 radiance spectra that belong to the cluster around \mathbf{r}_i .

Unfortunately, our initial implementation of spectral uncertainty contained a bug in the code, so the selected filters pair (Fig. 2) is not actually the best according to the described criterion. The bug has been spot long after the dataset was collected. In Fig. 11 we show the best filters selected by the criterion after the bug fix. We also probe those filters in simulated settings in Sec. A.5

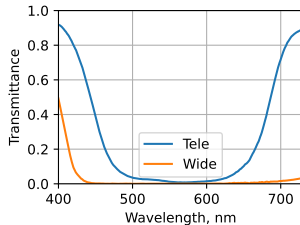


Figure 11: Best filters after the bug fix

Noise model. Let \bar{c}_i be a photometrically-normalized ground-truth signal level at channel i , t be exposure time, g be ISO. The expected collected charge at image sensor is $\bar{c}_i t$. Following Foi et al. [44], we model noise of the collected charge as $\varepsilon \sim \mathcal{N}(0, \alpha_i \bar{c}_i t + \beta_i)$, where α_i, β_i are parameters of the model. The final value in the raw image is further amplified by g along with the noise: $(\bar{c}_i t + \varepsilon)g$. Foi et al. also introduce additional noise after amplification, but we neglect it for simplicity. The observed photometrically-normalized signal is then given by:

$$c_i = \frac{(\bar{c}_i t + \varepsilon)g}{tg} = \bar{c}_i + \frac{\varepsilon}{t}.$$

To be consistent with (3) and (4), we define $\sigma_i(x)$ as:

$$\sigma_i(\bar{c}_i) = \frac{\sqrt{\alpha_i \bar{c}_i t + \beta_i}}{t} \quad (5)$$

We estimate parameters α_i, β_i of this model by plotting $\sigma_i t$ against $\bar{c}_i t$ in Fig. 12.

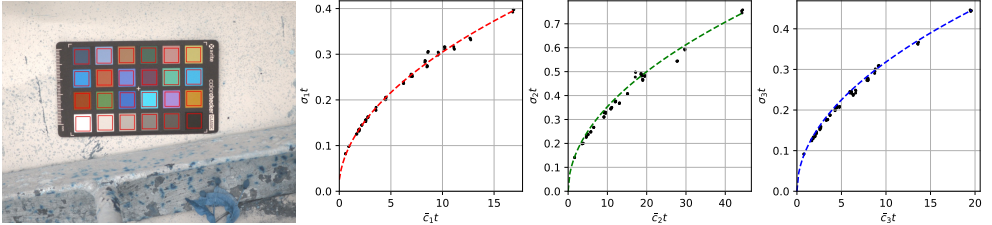


Figure 12: Plotting $\sigma_i t$ against $\bar{c}_i t$ for the Telephoto camera based on a single shot. Each data point (24 in total) is given by channel-wise mean and std dev of a color patch (left, in red). In each plot, point cloud is approximated by a dashed line (5) using least-squares; each color channel i gets its own noise parameters α_i, β_i (right).

The only problem left in (5) is the hidden dependence on t . Given simulated $\bar{\mathbf{c}} = \mathbf{S}_{\mathbf{F}} \mathbf{r}$, we cannot add noise properly unless we know exposure time t . In real-life setting, exposure time is determined by a camera automatically depending on the brightness of a scene. For simplicity, we model this in a piecewise-power fashion. We gathered 1000 raw images from phone’s gallery and plotted t against the average of photometrically normalized signals across all channels, height and width in an image $c = \frac{1}{h \times w \times 3} \sum_{i,j,k} \mathbf{I}(i, j, k)$ (Fig. 13). The fitted function allows to estimate t given \bar{c}_i .

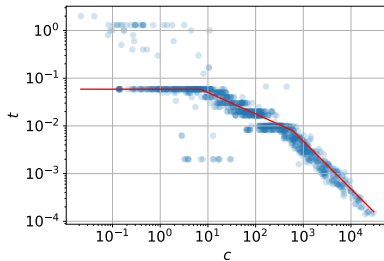


Figure 13: How exposure time depends on scene brightness. The piecewise-power function plotted in red line is used to model the exposure time given the average of a photometrically normalized image.

A.3 More on Doomer Dataset

In the full public release of Doomer dataset we will provide 3 main versions:

1. **RAW version.** Images from all cameras before any preprocessing.

2. **Single-camera version.** Pairs of a Main-camera photo and an HSI. The images are preprocessed and share the same FoV and spatial resolution.
3. **Multi-camera version.** Quadruples of Main-, Tele- and Wide-camera photos and HSI. The images are preprocessed and share the same FoV and spatial resolution.

Both the single- and multi-camera versions will also have two subversions depending on what spectral resolution of an HSI a user needs. Our resources allowed us to capture spectral radiance with the sampling interval of 3 nm. However, most of hyperspectral images have that of 10 nm as a compromise between precision and computational efficiency. A short summary of each version provided in Tab. 6. At the time of submission, only *emphasized* items are made available.

The preprocessing pipeline of RAW images consists of these steps: demosaicing, black current subtraction, flat field calibration and photometric normalization. For hyperspectral images, preprocessing pipeline includes: black current subtraction, flat field calibration, radial distortion correction and photometric normalization. The last step involves only division by the exposure time (Specim IQ has no ISO setting) and band-wise division by the calibration divisor \mathbf{k} .

Dataset version	Smartphone images	HSIs		FoV matching
		spectral range (step)		
RAW	Main, Tele, Wide	Original 400–1000 nm (3 nm)		–
1-camera	Preprocessed Main camera image	Preprocessed 400–730 nm (10 nm)	Preprocessed 400–730 nm (3 nm)	✓
3-camera	<i>Preprocessed and concatenated Main, Tele, Wide images</i>	<i>Preprocessed 400–730 nm (10 nm)</i>	Preprocessed 400–730 nm (3 nm)	✓

Table 6: Doomer Dataset versions

For all HSIs, we will provide a manually annotated binary mask that specifies the location of the gray ball. The reflectance spectrum of the gray ball, measured with the X-Rite spectrophotometer, will be included in the dataset. Also, we will expand it by adding more scenes and annotate each scene with tags depending on its contents.

Unlike previously published datasets, Doomer contains multiple real RGB images along with ground-truth HSI and illumination reference. This combination enables the exploration of various computational photography problems, such as:

1. *White point estimation* both in spectral and RGB forms.
2. *Illumination distribution estimation.* The need to estimate a distribution of illumination in a scene arises from the complexity of natural scenes. In such environments, a single global white point may be insufficient for accurate image processing and color correction [45].
3. *Color space transform.* Since there is a known white-point for each scene, it is possible to do precise chromatic adaptation and color signals for different cameras.

4. *Hyperspectral Reconstruction*. Reconstruction from single or multiple cameras. Reconstruction of different types of spectra — radiance or reflectance.

A.4 Rest of the MI-MSFN Architecture

Since the proposed neural network is rather a minor contribution and differs from MSFN only by the arrangement of blocks, we only gave a broad view on it in the main part of the paper. Some blocks were left unexpanded, which we fix by showing the missing details here in Fig. 14.

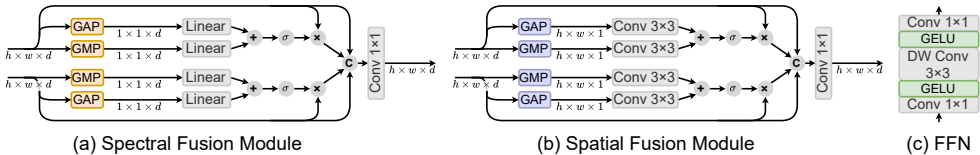


Figure 14: Illustration of fusion modules and feed-forward network in MI-MSFN. GAP and GMP stand for global average and max pooling respectively.

The remaining disambiguation consists of abbreviations expansion: S-MSA = spectral multihead self-attention [8]; SW-MSA = shifted window multihead self-attention [46]; W-MSA = window multihead self-attention [47].

A.5 Additional Experiments on Simulated Data

Having the estimated spectral characteristics of our filtered smartphone cameras setup (\mathbf{S}_F) and the sensor noise model (5), we find ourselves in a position, where we can simulate images of the triple-camera setup from HSIs and run experiments on simulated data. Unlike the real-life conditions, the simulated images are perfectly aligned to HSI and between each other. Evaluation on a simulated dataset then gives us a sight on how big the performance increase caused by the triple-camera setup could be if there was no misalignment at all. The results are shown in Tab. 7

Setting	PSNR, dB \uparrow	SAM, $^\circ$ \downarrow	NSE, % \downarrow
Single-camera	28.79 ± 0.46	5.40 ± 0.22	8.46 ± 0.37
Multi-camera	36.84 ± 0.39	2.69 ± 0.02	3.88 ± 0.06
Multi-camera (filters from Fig. 11)	37.90 ± 0.31	2.33 ± 0.06	3.43 ± 0.08

Table 7: Evaluations of MI-MSFN in single- and multi-camera settings on simulated data. Evaluation of the better filters combination is provided separately

The triple-camera setup in simulated conditions yields $\sim 50\%$ improvement in terms of SAM and NSE and $+8$ dB PSNR. Recalling the $\sim 30\%$ improvement in the real-life conditions, we can conclude that our results in the main part of the paper are reasonable.

Tab. 7 also includes results for the filters selected after we fixed the bug in our code (Fig. 11). It suggests that if we used those filters for the dataset collection, we could have achieved even better results on the real data in the main paper. Also, this simulation result strengthens the reasonableness of spectral uncertainty criterion.

A.6 Computational Resources

All the network trainings (Tab. 2, 3, 4) were executed on a cluster, allowing us to run up to 20 jobs in parallel. This was especially handy because we needed to run each experiment 10 times with different random seeds to ensure statistic significance. The cluster randomly assigned jobs to nodes, each having multiple GPUs. However, any job only used one GPU at a time. A GPU assigned to a job could be one of the following: NVIDIA L40, L40s and H100. Every training consumed < 23 GB of GPU memory and lasted no longer than 8 hours. 5 CPU cores were occupied by data loader; the total CPU memory consumption was < 8 GB.